# Molecular Beam Magnetic Resonance in Doped Helium Nanodroplets. A Setup for Optically Detected ESR/NMR in the Presence of Unresolved Zeeman Splittings†

**Markus Koch,*,§ Johannes Lanzersdorfer,§ Carlo Callegari,§ John S. Muenter,‡ and Wolfgang E. Ernst§**

*Institute of Experimental Physics, Graz University of Technology, Petersgasse 16, A-8010 Graz, Austria/EU, and Department of Chemistry, University of Rochester, Rochester, New York 14627-0216*

*Received: May 5, 2009; Revised Manuscript Received: July 21, 2009*

An apparatus is presented to perform magnetic resonance measurements in a beam of doped helium nanodroplets. This type of experiment faces the same difficulties as traditional molecular beam electric/magnetic resonance experiments, namely, an optically thin sample. Like many of these traditional experiments, it uses lasers to prepare the states of interest and to detect them after manipulation with a microwave field. Unlike these traditional experiments, Zeeman substates cannot be resolved by the laser transition because of the droplet-induced line broadening. A magnetic dichroism scheme is used instead, exploiting the favorable selection rules for the absorption of circularly polarized light. ESR spectra are shown for K atoms captured on the surface of He nanodroplets. The extension of the method to other atoms and molecules, and to NMR spectroscopy, is discussed.

## 1. Introduction

Since the first experiment in 1992,[1] the synergy of spectroscopy and helium droplets has produced outstanding results. Among them are the observation of effects directly linked to atomic-scale superfluidity[2,3] and the synthesis of highly unstable atomic[4] and molecular complexes.[5] In most cases, the experiments would have been impossible without some of the unique properties of these droplets, most notably their liquid state, low temperature (0.38 K, ref 6), inertness, and perfect isolation from one another.

A tightly closed shell atom, helium is spectroscopically silent up into the extreme ultraviolet. Atoms and molecules (dopants) individually captured by a helium droplet are thus an essential spectroscopic probe of the properties of the droplet. Conversely, the helium−dopant interaction is weak enough that high-resolution spectroscopy is still possible.[1−3,6,7] Contrary to initial expectations, the width of individual rovibrational lines is, in general, not lifetime-limited; thus, the line shape contains information on the interaction of the dopant with the droplet. In synthetic applications, high-resolution spectroscopy provides the necessary structural information on the complex being formed;[8] the limited loss of resolution allows the use of most of the spectroscopic schemes so successful in the gas phase. Among such schemes, the detection of microwave (MW) or radio frequency absorption via a coupled optical transition has played a major role in the direct measurement of fine and hyperfine structure. Shortly after the first application of lasers to spectroscopy, microwave−optical double resonance (MODR) was pioneered by Field et al.[9,10] Converting the resonance absorption of microwave photons into a change of optical signal observed either by laser-induced fluorescence[11] or by laser polarization[12] has enhanced the sensitivity by several orders of magnitude.

While in doped He droplets the electronic and rovibrational degrees of freedom are the best-investigated ones, this work focuses on the electron spin, and to a lesser extent nuclear spin, of dopants. As a probe, the spin turns out to be unaffected by the presence of the nonmagnetic helium, yet it is a fine indicator of the electronic structure of the dopant. Countless molecular beam electric/magnetic resonance (MBER/MBMR) experiments have been performed, starting from the pioneering work of Rabi and co-workers,[13−16] and all had to face the thin optical density of the sample. The impossibility of a direct absorption measurement was originally solved by deflecting atoms/molecules in specific quantum states using nonuniform fields. The state-selection deflecting field, or the *A* field, precedes the resonance region, or the *C* field. Finally, the quantum state distribution following the resonance region is analyzed in a second deflecting field, the *B* field. Atoms or molecules that follow the desired trajectories in the *A* and *B* fields (which can employ either magnetic or electric field gradients) are then detected to produce the desired spectroscopic signal. Historically, deflection MBER/MBMR experiments were applied to virtually all stable molecules, and today, the study of state-selected molecules in field gradients is experiencing a surge of popularity in relation to molecular deceleration.[17]

In order to enhance the sensitivity, the *A* field, *B* field, and beam detection steps have been replaced by laser beams in many modern experiments,[18−23] but the original nomenclature has remained. The so-called optically detected magnetic resonance (ODMR) method is based on the addressability of atom (or molecule) electronic states using single-frequency laser light, and spin-polarized atoms (or molecules) are produced by optical pumping.[24−26] In most of the MBER/MBMR experiments, the sharpness of spectral lines in the collisionless environment offered by a molecular beam allows state selection when applying a frequency-stabilized high-resolution laser. Schemes which additionally exploit selection rules normally do so to facilitate the assignment of complex spectra rather than to separate unresolved states.

† Part of the "Robert W. Field Festschrift".
* To whom correspondence should be addressed.
§ Graz University of Technology.
‡ University of Rochester.

10.1021/jp9041827 CCC: $40.75 
Published on Web 08/13/2009

The situation is radically different for dopants in/on helium nanodroplets; with notable exceptions, typical linewidths range from ~ 300 MHz ($10^{-2}$ $cm^{-1}$) for rotational[27,28] and rovibrational[6] transitions, to a few $cm^{-1}$ for electronic transitions of organic molecules,[2] to ~100 $cm^{-1}$ for atoms on the surface of the droplet,[29] and even more for atoms solvated inside.[30]

Stark-split lines in He nanodroplets have been seen in favorable cases of sharp lines of molecules with a large permanent electric dipole moment.[31] The large hyperfine structure of the NO molecule has been resolved,[32] but as a rule, Stark and Zeeman splittings have remained unresolved in He droplets.

As in traditional molecular beam experiments, the spin state of a system attached to He droplets can have indirect spectroscopic effects that are readily noticeable. One of them, the relation between relative intensities of rovibrational lines of high-symmetry molecules and nuclear spin states, is a classic of spectroscopy (ref 33 Chapter 1), best exemplified by molecules such as *para*-hydrogen, or $^{12}C^{16}O_2$, only having even rotational states. This effect has been repeatedly observed in He droplets,[34−39] but as it involves different nuclear spin multiplets rather than different spin projections in a quantizing magnetic field, it cannot be directly exploited in a nuclear magnetic resonance experiment.

Magnetic dichroism, that is, the magnetically induced dependence of the absorption properties of a sample on the polarization state of the exciting radiation, is also a classic of spectroscopy, which can be most favorably exploited when state resolution is not available;[40] for this reason, it is popular in matrix studies. In He nanodroplets, we have already exploited magnetic circular dichroism (MCD) to determine the electron spin temperature of alkali metal atoms and dimers[41,42] and to discriminate between spin−orbit splitting and Jahn−Teller distortion in trimers.[43] Here, we take it one step further and exploit it to implement ODMR in helium droplets.

## 2. Concept

In common with traditional molecular beam experiments, our method retains the use of optical transitions to "amplify" and make detectable the effect of a spin resonance transition. The modified ingredient is how state selection is accomplished (dichroism versus photon energy). The optical transition of choice is the main electronic transition of an alkali metal atom ($n^2P_{1/2,3/2} \leftarrow n^2S_{1/2}$, with $n$ as the ground-state principal quantum number), whose two spin−orbit split components are traditionally named $\mathbf{D}_1$ and $\mathbf{D}_2$ lines.

The influence of the He droplet on the valence electron gives rise to important facts to be considered. Investigations of K ($n = 4$) and Rb ($n = 5$) atoms on helium nanodroplets in magnetic fields of ~0.3 T have been carried out by our group, with the following findings:

(1) The lines of electronic transitions are broadened, as mentioned above, preventing the use of photon energy to select a specific spin state. Furthermore the selection rules for electronic dipole transitions are affected; thus, the addressability of spin states by use of circularly polarized light has to be verified. We found that for excitation energies near the $\mathbf{D}_1$ line, selection rules do remain sufficiently favorable[41,44] (see the MCD Measurements section).

(2) The spin population relaxation time $T_1$ has to be roughly known; depending on whether spin relaxation to the droplet temperature is fast or slow relative to the time-of-flight through the magnetic field, different experimental schemes are needed. In the first case, a spin polarization of the dopants occurs spontaneously; the $A$ field is not necessary, but the $B$ and $C$ fields must act simultaneously, that is, they cannot be spatially separated. In the second case, a circularly polarized laser beam is needed to produce a net spin unbalance, but the spin resonance and probing steps can be spatially separated. We found spin relaxation to be slow for atoms[41,44] and fast for dimers[41,42] and trimers.[43]

(3) Assuming optical addressability of the spin states and long $T_1$ times, two methods are possible to create a spin polarization, depending on the fate of the dopant upon excitation. It is known that some alkali metal atoms (K and smaller) always detach from the droplet upon excitation, while we found that Rb atoms may remain on the droplet under certain conditions.[44] In the first case, spin polarization is achievable by depletion of atoms with the unwanted spin orientation; in the second case, it is achieved by spin pumping. In both cases, a careful choice of the photon wavelength is required, within a range considerably narrower than the width of the broad electronic lines.[41,44]

MCD relates in the end to the fact that the photon carries an angular momentum (spin 1), with two possible orientations (parallel and antiparallel) of its projection onto the propagation direction; the photon is said to have positive or negative helicity, also indicated with the symbols $\sigma^+$ or $\sigma^-$, respectively. It is this angular momentum which combines with that of the atom being excited to give rise to selection rules and polarization-dependent absorption probabilities. Let us then briefly look at the angular momenta in an atom, restricting ourselves to our specific case of one valence electron and two electronic terms (the ground S state and the first excited P state) with the understanding that the concepts presented are of more general validity. Three angular momenta need to be considered, the orbital angular momentum of the electron, $\boldsymbol{L}$, its spin $\boldsymbol{S} = 1/2$, and the nuclear spin $\boldsymbol{I}$; these couple through the spin−orbit coupling constant $A_{SO}$ to give the total angular momentum of the electron $\boldsymbol{J} = \boldsymbol{L} + \boldsymbol{S}$ (for $\boldsymbol{L} = 0$, $\boldsymbol{J} = \boldsymbol{S}$) and the total angular momentum of the atom $\boldsymbol{F} = \boldsymbol{J} + \boldsymbol{I}$ through the hyperfine coupling constant $a_{HFS}$ ($a$ for brevity). Their projections along an external quantization axis (later to be defined by the direction of a static magnetic field, $B_0$) are indicated with $m_L$, $m_S$, $m_I$, $m_J$, $m_F$. At zero field, term levels are split chiefly by the spin−orbit interaction, except when this is strictly zero (in our case, for $\boldsymbol{L} = 0$) and only the hyperfine interaction contributes. In most cases, spin−orbit splittings remain resolvable in optical transitions in He droplets, but hyperfine ones do not. For this reason one has to resort to selection rules. For our application, the best description of the system remains that of an atom whose levels are shifted by the interaction with the droplet and may be mixed to a different extent. The rotational angular momentum of the doped droplet is neglected altogether. At least for electronic states of the dopant with $\boldsymbol{J} = 1/2$ (thus including the $^2S_{1/2}$ ground state and the $^2P_{1/2}$ component of the excited state doublet), it plays no significant role; for other excited states, the appropriate quantization axis for $\boldsymbol{J}$ is the normal to the droplet surface, and one can look at its instantaneous orientation relative to $B_0$.

The total angular momentum of $^{39}K$ (nuclear spin $\boldsymbol{I} = 3/2$; natural abundance: 93%) in its $^2S_{1/2}$ ground state can take the values $\boldsymbol{F} = 2$ and 1. The energy separation of these states at zero magnetic field corresponds to twice the value of the hyperfine coupling constant $a = 230.86$ MHz[45] (see upper panel of Figure 1). Both states are $2F + 1$ fold degenerate; applying an external magnetic field $B_0$ splits the individual levels according to their $m_F$ value. For weak fields, the shift is linear with $m_F$; the system is said to be in the Zeeman regime and is described in the $|\boldsymbol{J},\boldsymbol{I};\boldsymbol{F},m_F\rangle$ basis. At high field, $\boldsymbol{I}$ and $\boldsymbol{J}$ uncouple

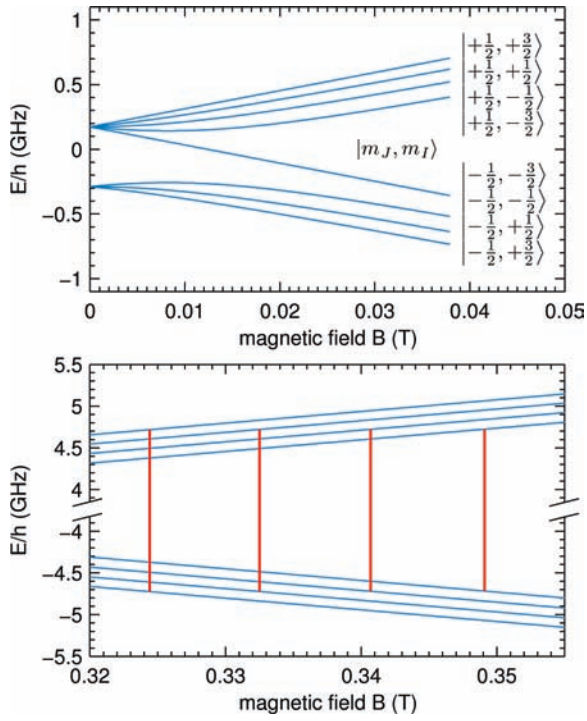


**Figure 1.** Upper panel: Energy diagram of the hyperfine levels of $^{39}$K in its electronic ground state ($^2S_{1/2}$) versus $B_0$, from the low-field (Zeeman) to the high-field (Back−Goudsmit) regime, as calculated with the Breit−Rabi formula.[16,46] Lower panel: Electron spin transitions $\Delta m_J = \pm 1$, $\Delta m_I = 0$ for a fixed MW frequency of $\nu = 9.44247$ GHz.

(Back−Goudsmit regime), and the shifts are again linear, this time separately in $m_J$ and $m_I$. The system is described in the $|\boldsymbol{J},\boldsymbol{I};m_J,m_I\rangle$ basis, and one speaks about electron spin transitions for $\Delta m_J = \pm 1$ and $\Delta m_I = 0$ and about nuclear spin transitions for $\Delta m_I = \pm 1$ and $\Delta m_J = 0$. Figure 1 (lower panel) shows the four electron spin transitions for a fixed microwave frequency of $\nu = 9.44247$ GHz, as presented in the Hyperfine-Resolved ESR Measurements section. At intermediate field strength, the energy levels are normally obtained by numeric diagonalization of the Hamilton operator; in the special case of $\boldsymbol{J} = 1/2$, the Breit−Rabi formula[16,46] (see the Appendix) provides an analytic solution, which is plotted in the upper panel of Figure 1.

Selection rules for absorption of a $\sigma^{\pm}$ circularly polarized optical photon are $|\Delta \boldsymbol{F}| = 1$, $\Delta m_F = \pm 1$ in the Zeeman regime and $|\Delta \boldsymbol{J}| = 1$, $\Delta m_J = \pm 1$ in the Back−Goudsmit regime. The use of these selection rules makes it possible to alter the populations in the electronic ground-state manifold. One can have either dissociation (for K) or relaxation back to the ground state (for Rb). In both cases, when the doped droplets exit the *A* field, they contain ground-state atoms whose population distribution of $m_F$ states has been altered, even if the Zeeman and hyperfine splitting of the ground state are not resolved. Note however that the presence of the droplet tends to mix the P states, which weakens the above effect. The effect of such a perturbation on MCD was measured and discussed by Islam et al.[47] as applying to CsAr van der Waals molecules. MBMR spectroscopy has been performed on the van der Waals molecules KAr (ref 48) and RbKr (ref 49). In our case, direct experimental tests (MCD Measurements section) prove that the droplet perturbation does not impair the applicability of the method. The same reasoning applies to the *A* field as that to the *B* field.

In the absence of further interaction, fluorescence at the *B* field location provides a baseline reference signal; now, MW radiation (the *C* field) is added between the *A* and *B* fields. Its magnetic component is perpendicular to the $B_0$ and induces electron spin transitions between Zeeman levels; the differential fluorescence signal between MW-on and MW-off as a function of the MW frequency $\nu$ (at fixed $B_0$) or, more commonly, as a function of $B_0$ at fixed $\nu$ provides a genuine magnetic resonance spectrum of the ground-state atoms (provided, of course, that the unbalance in the population distribution is sufficiently long-lived to survive the journey between the *A* and *B* fields).

## 3. Experimental Section

Helium droplets are produced in a standard helium droplet source (Figure 2). The direction of the droplet beam, the axis of fluorescence detection, and the direction of $B_0$ define, respectively, the *x*, *y*, and *z* axes of the laboratory frame of reference. The experiment is built around the MBER machine originally built in Rochester and presented in ref 50; the vacuum chamber and magnet have remained essentially the same, and a helium droplet source was built into the source chamber, which was fitted with a large unbaffled oil diffusion pump (NRC HS10, 4200 L/s nominal pumping speed) backed by a rotary/roots pump stack (Alcatel 2100 A, 100 m$^3$/h; Leybold RUVAC WS 500, 440 m$^3$/h). This kind of pumping speed is necessary to remove the large amount of gas released into the source chamber. The pickup chamber and detection chamber are equipped with turbo pumps (Leybold Turbovac 361, 400 L/s and Pfeiffer Vacuum TMU 521P, 520 L/s). Two laser beams, and the corresponding entrance and exit paths, a chopper, two pickup cells, a NMR magnetometer, a microwave cavity to increase the available MW power density of the *C* field, fluorescence collection optics at the location of the *B* field, a photomultiplier, and a surface ionization detector were also added to the design.

**3.1. Source and Doping.** The nozzle assembly is cooled by a two-stage closed cycle refrigerator (Leybold RW 4000 compressor; RGD 1245 cold head) capable of 12 W at 20 K and of a no-load minimum temperature of ≤10 K (nominal) at the second stage. The nozzle is suspended by fiberglass spacing discs inside of a copper cold shield which is thermally connected to the first stage of the refrigerator (45 W at 80 K, minimum temperature ≤ 35 K). The nozzle itself is a copper block (oxygen-free quality) with a thin long center hole into which high-pressure helium gas is fed. The gas line (1/8 in. copper tubing) is precooled at the first and second stages of the refrigerator, and a reduction (1/16 in. stainless steel tubing) between the two stages reduces the conductive thermal load. The nozzle is capped at the open end with a commercial electron microscope aperture (Günther Frey GmbH & Co., platinum disk 2.0 mm diameter, 0.6 mm thick, 5 $\mu$m nominal aperture diameter). A sintered filter (Swagelock, 2 $\mu$m pore size) is embedded in the nozzle to prevent clogging of the orifice. A supersonic expansion into vacuum occurs through this orifice; the center portion of the droplet beam thus formed passes through a commercial electroformed skimmer (Beam Dynamics, model 2, 300 $\mu$m diameter) and enters the doping chamber. For trajectory tracing purposes, the droplet beam can be described as the geometric projection of a point source through the skimmer aperture. Thermal contraction during cool down demands that adjustment of the orifice position in the $y-z$ plane be possible from outside of the source chamber. There is no provision to change the nozzle-to-skimmer distance during operation; its value is fixed at 13 mm for all experiments. The nozzle manipulator is rigidly connected to the cold shield of the nozzle via a thin-walled stainless steel tube to suppress heat

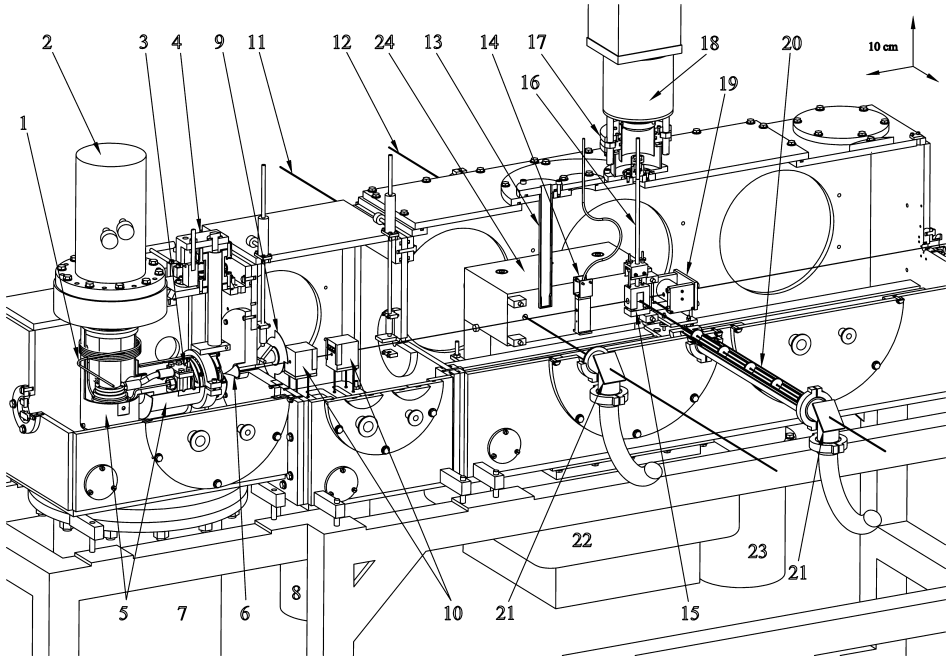


**Figure 2.** The He droplet magnetic resonance machine (cutout). 1: Helium gas line. 2: Closed cycle refrigerator (cold head). 3: Nozzle assembly. 4: Nozzle manipulator. 5: Cold shields. 6: Skimmer. 7: Diffusion pump (source chamber). 8: Turbo pump (pickup chamber). 9: Droplet beam chopper. 10: Pickup cells. 11: Pump laser beam (*A* field). 12: Probe laser beam (*B* field). 13: Magnetometer head. 14: Microwave cavity (*C* field). 15: Two-mirror laser-induced fluorescence collector. 16: Light guide. 17: Light-tight mating tube. 18: Peltier-cooled photomultiplier housing. 19: Surface ionization detector. 20: Baffled exit path of laser. 21: Brewster angle exit windows. 22: Electromagnet coils. 23: Turbo pump (detector chamber). 24: Electromagnet pole piece. Note the length scale on the top right corner.

transfer. To thermally connect the nozzle and its cold shield to the second and first stages of the refrigerator, respectively, flexible copper braids (70 $mm^2$ cross section) with crimped end pieces are used. Mating surfaces, which are polished with diamond paste, are held in tight contact by screws. Thermal contact is augmented by a thin layer of Apiezon-N grease (Apiezon Products Ltd., London, U.K.), whose merits are quantitatively analyzed in ref 51. The lowest attained nozzle temperature is 9 K, and a typical cool down time to 10 K is 90 min. For temperature stabilization, the voltage drop across a silicon diode (DT-670, Lake Shore Cryogenics, Inc.), fed with 10 $\mu$A, serves as the input of a PID controller (Eurotherm, model 3500), which powers a 75 Ω, 10 W resistor. The nozzle temperature can be set from 9 to 30 K, with maximum fluctuations of 20 mK. Electrical connections are made with thin magnet wires, which are thermally anchored using metal-filled epoxy resin.

The droplet beam may be mechanically chopped (Figure 2, item 9) for differential laser-induced fluorescence (LIF) and MCD measurements (see below). The droplets then pass through two sequential pickup cells, with 2 mm diameter entrance and exit holes, where they may collide with atoms and become doped. The cells are filled with a few grams of the alkali metal of choice (here K and Rb) and can be electrically heated. The partial pressure of the atomic vapor inside of each cell is controlled via the cell's temperature. In the experiments presented here, only one cell at a time is heated. Typical temperatures to maximize the number of single-atom-doped droplets are 115 °C for K and 85 °C for Rb.

**3.2. Detection.** The doped droplets then enter the detection chamber and the gap of a custom-made electromagnet (Pacific Electric Motor Co., 2 × 324 turns) with the following characteristics: pole pieces: 12 in. length, 4 in. height, 1 in. gap; capable of ∼0.8 T at 60 V, 80 A. The magnet is energized by a stabilized power supply (FUG NTN 700-125) operating in constant current mode; small removable scanning coils (not shown in Figure 2) are wound next to the main coils and allow sweeps of ∼10 mT in steps of typically 0.3 $\mu$T. They are energized by a small voltage-controlled power supply (0−32 V, 0−10 A). $B_0$ is measured with a NMR magnetometer (Drusch RMN2) a few cm upstream of the cavity location and above the droplet beam, with a nominal precision of ±0.3 $\mu$T and an accuracy of ±0.4 mT. The latter limit essentially originates from slight magnetic field gradients which also appear to set the limit for the observed linewidth. More accurate measurements are made by using the ESR lines from gas-phase atoms directly effusing from the pickup cell as markers (see below). Depending on the excitation and detection scheme used, several experiments are possible. ODMR uses the whole setup and will be described first.

***3.2.1. ODMR Scheme.*** The droplet beam crosses in sequence the *A* field preparation laser beam, the *C* field X-band MW cavity (homemade, 22.9 × 10.2 × 65.0 $mm^3$, $TE_{103}$ mode, resonant frequency $\nu_0 = 9.442$ GHz, *Q* factor: ∼5000), and the *B* field probe laser beam. The LIF signal is generated by the circularly polarized probe laser beam in dependence of the alkali metal electron spin state, and emitted photons are detected with a photomultiplier tube (Burle C31034A; Housing: Products for Research TE104 TS RF). The pulses from the photomultiplier tube are discriminated and amplified (model 9302, Ortec) and counted with a homemade four-channel counter, the exact counting scheme depending on the experiment being performed. Fluorescence is collected with a homemade, high numerical aperture, two-mirror arrangement and funneled into a light guide (glass, 1/4 in. diameter, American Optical Corporation), which leads the light to the photomultiplier outside of the detection chamber. The two mirrors are arranged such that the center of the spherical (upper) mirror and one focal point of the ellipsoidal (lower) mirror coincide with the crossing point of the laser and droplet beam. The entrance surface of the light guide is located in a recess of the crown of the spherical mirror, at the position of the second focal point of the ellipsoidal mirror. Light emitted

into the upper hemisphere is retro-reflected, and light entering the lower hemisphere is focused into the light guide. Both mirrors are made of solid aluminum, machined with a CNC lathe, and polished with diamond paste. A separate test of this setup found its overall efficiency to be up to 36% (the amount of laser light scattered into the full solid angle by a nylon screw (mimicking the droplet beam) was compared with the amount of light at the exit end of the light guide).

The *A* and *B* field lasers enter and exit their respective interaction regions via 10 mm holes drilled through the magnet pole pieces. The laser beams are obtained by splitting the output of a cw Ti:$Al_2O_3$ ring laser (Coherent, Inc., 899-01 series). It is particularly critical to keep scattered light at the *B* field location as low as possible; therefore, the *B* field laser beam enters the vacuum chamber through a stack of five baffle apertures. These have carefully sharpened edges and are thoroughly blackened; their open diameters are 6.0/5.3/4.5/3.7/3.0 mm (sequence as seen by the incoming laser beam), they are separated from one another by 103 mm, and the last one is 202 mm away from the two-mirror arrangement. Likewise, the baffle tubes and the holes through the magnet are also blackened; additional apertures (open diameters of 7.0 and 8.0 mm) are placed near the collecting mirrors to restrict as much as possible their field of view. The *A* and *B* laser beams propagate parallel or antiparallel to the magnetic field and are circularly polarized, with same helicity, using Pockels cells operated at 2.5 kV. The laser is tuned to the $\mathbf{D}_1$ line of the target atom, the exact photon energy within the droplet-broadened peak being chosen such that the spin polarization action of the pump beam is most efficient. This is assessed by monitoring the amount of MCD signal in the absence of a *C* field (see the MCD Measurements section).

The beam of a single-frequency grating-stabilized diode laser with a tapered amplifier system (TA 100, Toptica Photonics AG) tuned to the $\mathbf{D}_1$ line of the gas-phase atom (K: 12985.170 $cm^{-1}$; Rb: 12578.950 $cm^{-1}$; ref 52) is split and polarized in the same fashion and serves to generate the marker ODMR signal from gas-phase atoms effusing from the pickup cell. Unlike their counterparts on He droplets, electronic transitions of free atoms are hyperfine-resolved, meaning that the single-frequency diode laser must, in principle, be stabilized within the narrow natural linewidth (~10 MHz) of a specific transition. If measurement time is not of concern, it is also possible to scan through the hyperfine transition of interest and record the integrated signal; this is currently our scheme of choice. The diode laser is operated at a power of ~2 mW.

The single-frequency MW *C* field is generated by a synthesizer/amplifier combination (HP83620A/HP8348A, Hewlett−Packard). A circulator (model 4925, Narda) is used to adjust the synthesizer to the resonant frequency of the cavity by minimizing the reflected signal of the cavity. A semirigid coaxial cable (RG402/U, 50Ω) of 0.8 m length is used to guide the MW into the detection chamber and directly couple it into the cavity by the method of loop coupling.[53] It is worth noting that the gas leakage rate through this length of cable is sufficiently low that no additional vacuum feedthrough is required. The entrance and exit holes for the droplet beam are at the standard location for a rectangular ESR cavity, where the magnetic component $B_1$ of the *C* field has an antinode to maximize signal and the electric component has a node to minimize radiation losses. $B_1$ is linearly polarized along *x*.

ESR transitions are recorded by scanning $B_0$. The *C* field is modulated on and off at 19.4 Hz, and the LIF photons are counted for 20 ms during the on-phase ($N_{on}$) and the off-phase ($N_{off}$). This gating time is intended to suppress possible fluctuations at 50 Hz (the power line frequency) and is intentionally shorter than the chopper-open (chopper-closed) interval, so as to eliminate counts at the modulation edges. $B_0$ is scanned in steps, and at each step, $N_{on}$ and $N_{off}$ are accumulated over a total gating time of 1 s each. Their difference, $N_{diff} = N_{on} - N_{off}$, is the ESR signal which increases when the *C* field is resonant with a spin transition of the alkali metal atoms.

***3.2.2. LIF and Beam Depletion (BD) Schemes.*** The experimental apparatus offers the possibility of recording excitation spectra of alkali-metal-doped helium droplets by the standard methods of LIF[54] and beam depletion (BD),[55] for which the *B* field alone is necessary.

The scheme is the same as that presented in ref 42. For LIF spectra, the droplet beam is chopped in the pickup chamber at 19.4 Hz, and each channel of the counter is synchronously gated for exactly 20 ms. In analogy to the ESR signal, counts are accumulated for 1 s each, and the difference of the two channels is the LIF signal.

For BD spectra, the droplet beam is continuous, and the laser beam is chopped instead before entering the vacuum chamber. The current signal from the surface ionization detector, which is proportional to the number of alkali metal atoms reaching the detector, is amplified with a picoammeter (Keithley, model 485) and measured with a lock-in detector; when the laser is resonant with an electronic transition, the excited alkali metal atoms detach from the droplet, and the event is recognized as a decrease of this signal.

***3.2.3. MCD Scheme.*** For a MCD spectrum, the *A* and *B* field laser beams are needed. Ideally, these would come from two independently tunable sources, so that the effect of the photon energy on the preparation and detection steps could be independently investigated. The need for high power forced us to split them out of the same beam from the Ti:$Al_2O_3$ laser. The *A* field laser beam is $\sigma$ polarized and has a power of typically 1 W; the *B* field beam has a power of 0.1 W. The polarization of the *B* field is modulated between $\sigma$ (same helicity as the *A* field laser beam) and linear at half of the chopping frequency (modulation between $\sigma^-$ and $\sigma^+$ is not possible for technical reasons). A four-channel counting scheme is used. Photons are counted for one chopper on-and-off period with linear polarization, giving the differential signal $N_l$, and subsequently for another on-and-off period with $\sigma$ polarization, giving the differential signal $N_\sigma$. A MCD signal is formally proportional to the population difference of the $m_J = -1/2$ and $+1/2$ ground states; how these are related to $N_\sigma$ and $N_l$ depends on the degree of saturation of the *A* and *B* field transitions and on the validity of the selection rules. It is not easy to quantitatively account for these factors in our measurement; in any case, the strength of the signal $N_l - N_\sigma$, which we will improperly call an MCD spectrum, is a direct indicator of the most suitable photon energy to perform the ODMR measurements and, if compensated for the transition strength via the intensity of the LIF spectrum, is also a good indicator of where selection rules do hold best.

## 4. Results

**4.1. LIF and BD Measurements.** The amount of available LIF signal is an important parameter of the ODMR scheme; therefore, its variation as a function of droplet size was investigated first. Figure 3 shows the LIF signal (*B* field laser at 75 mW, linearly polarized) for a fixed photon wavenumber of 13005 $cm^{-1}$, approximately the maximum of the $\mathbf{D}_1$ peak. Data were sampled at all possible combinations of nozzle temperatures $T_0$ from 10 to 30 K (in 1 K steps) and pickup cell

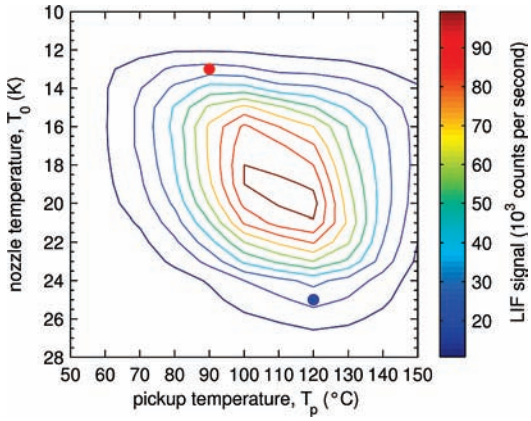


**Figure 3.** LIF signal for different combinations of nozzle temperatures $T_0$ and pickup temperatures $T_p$ at fixed $p_0 = 50$ bar. The *B* field laser (linearly polarized at a power of 75 mW) is tuned to the maximum of the $\mathbf{D}_1$ transition of K atoms on a droplet (13005 $cm^{-1}$). Contour lines go from 10000 (outermost) to 100000 (innermost) counts per second in steps of 10000 counts per second. The two dots mark the $T_0 - T_p$ combinations representative for small (blue) and big (red) droplets. BD and LIF spectra with these parameters are shown in Figure 4.

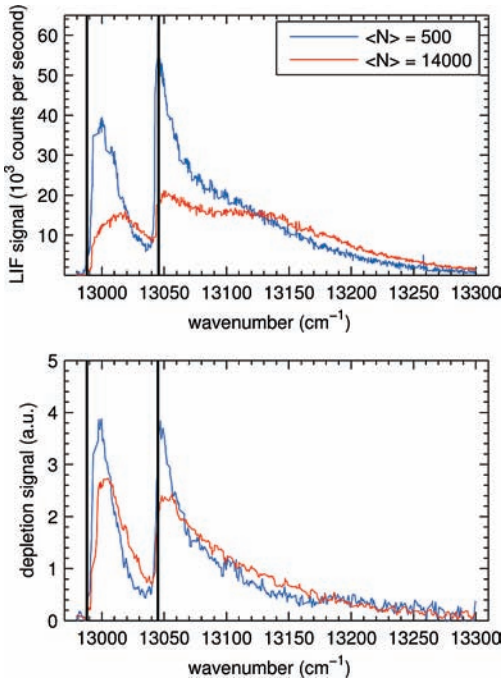


**Figure 4.** LIF spectra (upper panel) and BD spectra (lower panel) for K at different droplet sizes. Blue lines: small droplets with an average droplet size of $\langle N \rangle = 500$ (blue dot in 2: $T_0 = 25$ K and $T_p = 120$ °C, K partial pressure: $6.1 \times 10^{-5}$ mbar). Red lines: big droplets, $\langle N \rangle = 14000$ (red dot in 2: $T_0 = 13$ K and $T_p = 90$ °C, K partial pressure: $1.4 \times 10^{-5}$ mbar). The black bars mark the positions of the gas-phase $\mathbf{D}_1$ and $\mathbf{D}_2$ transitions at 12985.17 and 13042.89 $cm^{-1}$, respectively. The two BD spectra have been normalized to have the same integrated area, and the corresponding LIF spectra have been scaled accordingly.

temperatures $T_p$ from 50 to 150 °C (in 10 °C steps). The latter range corresponds to calculated equilibrium vapor pressures $p_p$ from $4.2 \times 10^{-7}$ to $7.7 \times 10^{-4}$ mbar for K. The stagnation pressure $p_0$ in the nozzle was, as for all experiments presented here, 50 bar.

Low $T_0$ results in relatively few droplets, of large size, requiring a low partial pressure in the pickup cell and thus a low $T_p$. Increasing $T_0$ gives more droplets, of smaller size, increasing the required $T_p$ and giving a higher overall LIF signal. The maximum LIF signal at around $T_0 = 19$ K and $T_p = 110$ °C corresponds to a droplet size of approximately 3700 helium atoms [ref 56; since no droplet sizes for the nozzle pressure that we used (50 bar) are reported, those at the closest available value (40 bar) are taken]. Since the full width at half-maximum of the droplet size distribution approximately equals the mean droplet size,[56] higher values of $T_0$ deliver a significant number of droplets that are too small. This effect decreases the obtained LIF signal for $T_0$ above ~20 K. Let us note here that the maximum of the $\mathbf{D}_1$ peak does shift with droplet size, so that the data shown in Figure 3 may have been measured slightly off the maximum. Furthermore, the $\mathbf{D}_1$ line and the red-most part of the $\mathbf{D}_2$ line, corresponding largely to exciplex formation, are likely underrepresented for bigger droplets. Both effects are discussed in the following paragraphs.

The influence of the droplet size on the whole excitation spectrum is shown in Figure 4. LIF and BD spectra are taken for small droplets with an average droplet size of $\langle N \rangle = 500$ (blue trace) and for big droplets with $\langle N \rangle = 14000$ (red trace). The corresponding $(T_0,T_p)$ coordinates are indicated in Figure 3 as a blue dot (small droplets, $T_0 = 25$ K and $T_p = 120$ °C, $p_p = 6.1 \times 10^{-5}$ mbar) and a red dot (big droplets, $T_0 = 13$ K and $T_p = 90$ °C, $p_p = 1.4 \times 10^{-5}$ mbar).

For the sake of comparison, the two BD spectra have been normalized to have the same integrated area, and the corresponding LIF spectra have been scaled accordingly. This is justified by the fact that the BD signal delivers an undistorted absorption spectrum (provided, as is the case, that excitation always results in depletion), whereas the LIF signal additionally depends on the wavelength of the emitted photon due to the spectral response of the photomultiplier tube. LIF spectra of K atoms on droplets have been analyzed in the literature in great detail.[29,57−59] In short, the system is described as a diatomic molecule with the dopant playing the role of the second atom. Electronic states are labeled with the standard Hund's case (a) notation $^{2S+1}\Lambda_\Omega$, with $S$ being the spin, $\Lambda$ the projection of the orbital angular momentum onto the "molecular axis", and $\Omega$ the projection of the total electronic angular momentum onto the same axis. Taking spin−orbit coupling into account, the first excited atomic state, $^2P_{1/2}$, becomes a $^2\Pi_{1/2}$ state. The atomic $^2P_{3/2}$ state is split into a $^2\Pi_{3/2}$ and a $^2\Sigma_{1/2}$ state, with the first being slightly lower in energy. It is known that fluorescence emission occurs after atoms have detached from the droplet and that two detachment channels exist, one in which the atoms desorb alone and the other where they drag along one He atom (less likely, two or more) and form an exciplex. Exciplex fluorescence is shifted to the red of the excitation wavenumber by ~1000 $cm^{-1}$ per He atom,[29,57] with the result that K−He emission lies at the lower end of the sensitivity range of the photomultiplier tube and that $K-He_2$ is completely below. Thus, the exciplex channel is weighted correspondingly less than the free-atom channel. Excitations into the $^2\Pi_{1/2}$ state and into the $^2\Pi_{3/2}$ state have a large branching ratio into the excimer channel; the significant reduction of the intensities of these peaks in the LIF spectrum of large droplets suggests that this branching ratio strongly depends on droplet size.

Droplet-size-dependent LIF spectra have previously been recorded for Na and Li atoms[29] only. While for Li no significant effect was observed, for Na atoms, increasing the cluster size results in a slight blue shift of the $\mathbf{D}_1$ line, as well as substantial overall broadening of the transition. Due to smaller spin−orbit coupling, the $^2\Pi_{1/2}$, $^2\Pi_{3/2}$, $^2\Sigma_{1/2}$ states are not fully distinguishable, and an increased branching ratio into the excimer channel would merely emphasize the blue wing of the peak, thus being observed as an overall line broadening.

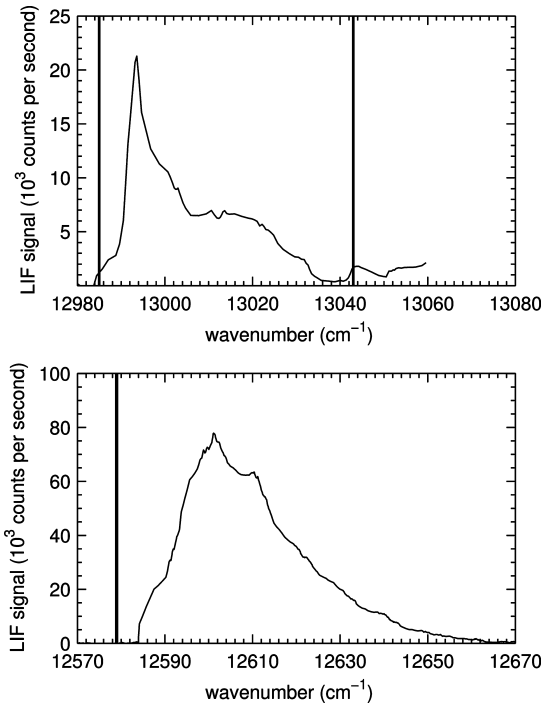


**Figure 5.** MCD spectrum of K (upper panel) and Rb (lower panel). As explained in the main text, the spin polarization and spin probe action are most efficient at the maximum of the MCD signal (12993 $cm^{-1}$ for K and 12601 $cm^{-1}$ for Rb). The black bars mark the positions of the gas-phase $\mathbf{D}_1$ and $\mathbf{D}_2$ transitions. These spectra are very sensitive to fluctuations of laser power, and small secondary maxima such as the one at about 12610 $cm^{-1}$ are instrumental artifacts.

**4.2. MCD Measurements.** Figure 5 shows the MCD spectra for K (upper panel), which are compared to those of Rb (lower panel).

Two effects induced by the droplet on the dopant combine to dictate the intensity of the MCD signal as a function of wavenumber, how the transition strength is spread and how selection rules are spoiled by the interaction of the atom with the helium. The transition strength can be determined by the well-known LIF spectra[29,60] and is peaked a few tens of wavenumbers above the gas-phase lines. As a qualitative estimate for the selection rules, one can say that the higher the excitation energy, the stronger the instantaneous interaction with the droplet in the excited state, and thus the stronger the droplet-induced quenching of the spin−orbit interaction and hence the MCD intensity.

This qualitatively explains the shape of the MCD spectra for K and Rb. In the case of Rb, spin−orbit splitting is large, and the transition strength factor dominates; the peak of the MCD spectrum practically coincides with that of the LIF spectrum (at high laser power, this is amplified by the possibility of multiple excitation−relaxation cycles,[44] which is more favorable for lower excitation energy). In the case of K, it is convenient to trade some transition strength in exchange for more favorable selection rules, and the MCD signal peaks at significantly lower excitation energy than the LIF peak. The spin polarization and spin probe action are most efficient at the maximum of the MCD signal, 12993 $cm^{-1}$ for K and 12601 $cm^{-1}$ for Rb. Both values, as well as the overall shape of the spectra, agree with former results[41,44] obtained from one-laser experiments.

**4.3. Hyperfine-Resolved ESR Measurements.** The MW frequency used ($\nu$ = 9.44247 GHz) requires a corresponding $B_0$ on the order of 0.3 T. In this region, $^{39}$K is in the Back−Goudsmit limit, and the value of the hyperfine line splitting approaches $a$. The lower panel of Figure 1 shows the four computed $\Delta m_J = \pm 1$, $\Delta m_I = 0$ transitions, and the corresponding multiplet is indicated in Figure 6 (upper panel). The lines can be thought of as electron spin transitions in the slightly different magnetic field associated with each possible orientation of $\boldsymbol{I}$.

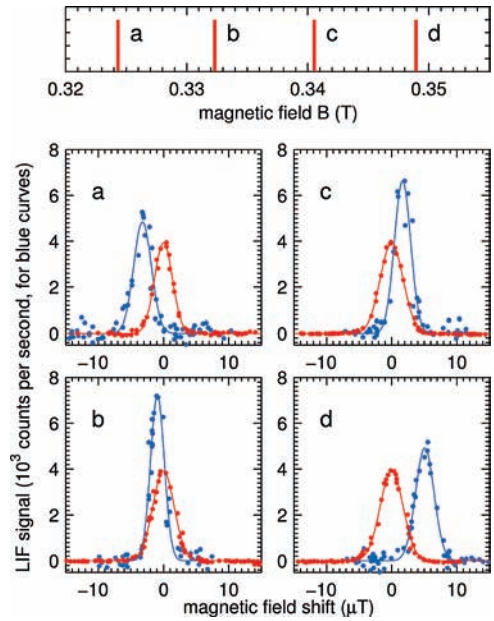


**Figure 6.** Multiplet with the four electron spin transitions ($\Delta m_J = \pm 1$, $\Delta m_I = 0$) of $^{39}$K, as indicated in the lower panel of Figure 1. Upper panel: Positions calculated with the Breit−Rabi formula. Four lower panels: Shifts of the ESR peaks of atoms on droplets (blue) with respect to the free atom (red). The lines are Gaussian fits of the measured data (dots). The free-atom data were measured directly as an analogue current signal from the photomultiplier and are plotted in arbitrary units, after subtraction of the baseline value.

The red data points in Figure 6 (four lower panels) are obtained from free atoms using the single-frequency diode laser tuned to the sharp free-atom line. The data are fitted with a single Gaussian peak whose center gives the exact value of $B_0$ in the microwave cavity for each transition. The blue data points (similarly fitted) originate from atoms on droplets and are obtained with the Ti:$Al_2O_3$ ring laser tuned to the maximum of the $\mathbf{D}_1$ doped droplet line. The free-atom data are plotted in arbitrary units and were measured directly as an amplified analogue signal from the photomultiplier (the baseline value is subtracted). Because the lines overlap, the two lasers must be used in sequence. For Rb atoms, the droplet-induced line shift is bigger (due to a higher value of $a$), which allows one to record both peaks simultaneously, upon superimposing the Ti:$Al_2O_3$ and the diode laser beams.

The position of the lines can be modeled with the Breit−Rabi formula[16,46] (see the Appendix), which is parametrized with the electron and nuclear $g$ factors ($g_J$, $g_I$, respectively) and the hyperfine constant $a$. Knowing $B_0$ from the free-atom transitions, the lines observed on droplets are modeled with the Breit−Rabi formula by using the variations $\delta g_J$, $\delta a$ ($g_I$ is kept unchanged) from the free-atom value[45] as free parameters. Table 1 lists the measured line positions, given by the NMR magnetometer as calibration, together with the ones calculated for free atoms, from known atomic constants. Each value is averaged over a minimum of two scans. The rather large difference between the calculated and measured values is due to the magnetic field inhomogeneity, compounded with the spatial separation between the MW cavity and the NMR magnetometer, and shows the

**TABLE 1: $^{39}$K ESR Transitions of Free Atoms and Atoms on Helium Droplets**

| transition | | free atoms | | | | fwhm | |
|---|---|---|---|---|---|---|---|
| $\|m_J'',m_I''\rangle$ | $\|m_J',m_I'\rangle$ | calculated (T) | measured (T) | on droplet measured (T) | shift ($\mu$T) | free atom($\mu$T) | on droplet ($\mu$T) |
| $\|+1/2, +3/2\rangle$ | $\|-1/2, +3/2\rangle$ | 0.3244255 | 0.3243223(1) | 0.3243191(1) | −3.2(1) | 3.1(1) | 3.0(1) |
| $\|+1/2, +1/2\rangle$ | $\|-1/2, +1/2\rangle$ | 0.3324629 | 0.3323171(1) | 0.3323161(1) | −1.0(1) | 4.0(1) | 3.0(2) |
| $\|+1/2, -1/2\rangle$ | $\|-1/2, -1/2\rangle$ | 0.3407018 | 0.3405325(1) | 0.3405345(1) | +2.0(1) | 4.1(1) | 2.9(2) |
| $\|+1/2, -3/2\rangle$ | $\|-1/2, -3/2\rangle$ | 0.3491424 | 0.3489385(1) | 0.3489436(1) | +5.0(1) | 4.4(1) | 3.0(1) |

necessity of the free-atom transition as a marker. Modeling the transitions on droplets results in a $g$ factor variation $\delta g_J = -3 \pm 2$ ppm and a hyperfine constant variation $\delta a = 335 \pm 60$ ppm. A second series of measurements gave the same results, $\delta g_J = -5 \pm 1$ ppm and $\delta a = 315 \pm 50$ ppm. We therefore conclude that the electron $g$ factor remains practically unchanged, and the hyperfine constant is increased, on average, by $325 \pm 40$ ppm. Similar conclusions for the values of $\delta g_J$ and $\delta a$ are reached for Rb, where more favorable experimental details allow us to even follow $\delta a$ as a function of droplet size. The physical origin of the change of $a$, which has been elucidated in detail by Adrian[61] for H atoms trapped in rare gas matrixes, lies in how the interaction between the droplet and the alkali metal atom affects the valence electron wave function of the latter. At short range, Pauli exclusion forces dominate and tend to increase the electron density at the position of the nucleus, thus the Fermi contact interaction and the hyperfine splitting. At long range, van der Waals interactions have the opposite effect; the balance of this partial cancellation is, in our case, positive. An excerpt of this rich set of data has been presented in ref 62, and a detailed analysis will be published separately.

The theoretical limit on the linewidth is given by the transit time through the microwave cavity ($\tau_t \approx 60\ \mu s \equiv 0.7\ \mu T \equiv 20$ kHz); therefore, there is an ample margin of resolution to observe hyperfine multiplets. Let us note that the linewidth, although extremely sharp ($\sim 3\ \mu T \equiv 84$ kHz, for a relative linewidth of $\sim 1 \times 10^{-5}$) is much broader than the instrumental limit. We have ruled out significant power broadening and concluded that the main source of broadening is a gradient of the static magnetic field.

Because of the coherent nature of the electron spin transition, the maximum height of the line versus microwave power displays the expected pattern of Rabi oscillations.[62] The envelope of the oscillations is affected by the aforementioned static magnetic field gradients; this is currently being investigated in detail.

## 5. Summary and Conclusions

In summary, we present an apparatus to perform ESR of doped helium nanodroplets, achieved by optically detected magnetic resonance (ODMR). The yield of laser-induced fluorescence (LIF) is first measured for a broad range of nozzle and pickup conditions, and the influence of droplet size on LIF and beam depletion (BD) spectra is shown. A magnetic dichroism scheme is used to overcome the problem of unresolved Zeeman splittings. The optimum wavelength for the spin polarization and spin probe of K and of Rb atoms is assessed through magnetic circular dichrosim (MCD) spectra; it turns out that the choice of laser wavelength critically determines the efficiency of the overall scheme. Hyperfine-resolved ESR spectra of $^{39}$K atoms on helium nanodroplets demonstrate the capabilities of the apparatus. In particular, we find a droplet-induced change of the hyperfine constant of $\delta a = 325 \pm 40$ ppm, whereas the electron $g$ factor remains practically unchanged.

Through the link between the above quantities and the electronic wave function of the alkali metal atom, as well as through direct spin−spin interaction, the method provides the possibility of accurate measurement of environmental effects, such as the interaction with another dopant. Almost invariably, the latter will be solvated inside of the droplet; thus, the droplet size is a convenient handle to control the distance between the two interacting partners. Spin labeling of ESR-silent species, spin exchange with magnetic nuclei (such as $^{129}$Xe), and the study of magnetically active materials of great technological importance, such as Cr and small clusters thereof, will all be relatively easy to achieve with our method. A pickup cell for gaseous species and a source for high-melting materials, based on electron impact heating, are currently being built. The accuracy of the instrument will also be increased by incorporating a NMR sensor directly into the microwave cavity and by adding shimming coils to cancel out magnetic field gradients. Adding radio frequency coils will easily make the method applicable to NMR transitions.

**Acknowledgment.** The authors gratefully acknowledge stimulating discussions with Gerald Auböck and thank Christian Neureiter for technical support, as well as Udo Buck for donating the closed cycle refrigerator. This research is supported by the Austrian Science Fund (FWF) under Grant P18053-N02.

## Appendix

**Mathematics.** In order to derive the Breit−Rabi formula, it is convenient to work in the uncoupled basis $|\boldsymbol{J},\boldsymbol{I};m_J,m_I\rangle$, where the interaction with the magnetic field is diagonal and given by:

$$E_{unc} = (g_J m_J + g_I m_I)\mu_B B \quad (1)$$

$$= W\left(m_J + \frac{g_I}{g_J - g_I} m_F\right)x \quad (2)$$

with

$$x = \frac{(g_J - g_I)\mu_B B}{W} \quad (3)$$

where the dimensionless quantity $x$ is roughly the Zeeman splitting of the uncoupled system measured in units of the zero-field hyperfine splitting $W = a(I + 1/2)$, $a$ being the hyperfine coupling constant. Hyperfine coupling $a\boldsymbol{I} \cdot \boldsymbol{J}$ introduces off-diagonal terms, whose evaluation can be simplified in terms of the following identities: $2\boldsymbol{I} \cdot \boldsymbol{J} = \boldsymbol{F}^2 - \boldsymbol{I}^2 - \boldsymbol{J}^2 = I_+J_- + I_-J_+ + 2I_zJ_z$, either using Clebsch−Gordan coefficients and the fact that $\boldsymbol{I} \cdot \boldsymbol{J}$ is diagonal in the coupled basis $|\boldsymbol{J},\boldsymbol{I};\boldsymbol{F},m_F\rangle$ or using the standard formulas for the ladder operators $I_\pm$, $J_\pm$ (see, e.g., ref 63). Because $m_F = m_I + m_J$ remains a good quantum number, this can only couple states with the same $m_F$; in particular, the

two states with maximum $|m_F|$, that is, $|\boldsymbol{J},\boldsymbol{I};+J,+I\rangle$, $|\boldsymbol{J},\boldsymbol{I};-J,-I\rangle$, do not mix at all, and their energy is a linear function of the magnetic field (eq 7). In the special case of $J = 1/2$ ($m_J = \pm 1/2$) considered here, only pairs of states $|\boldsymbol{J},\boldsymbol{I};+1/2,m_F - 1/2\rangle$ $|\boldsymbol{J},\boldsymbol{I};-1/2,m_F + 1/2\rangle$ will be mixed, and the matrix form of the hyperfine coupling $2 \times 2$ blocks is:

$$E_{\mathrm{HFS},m_F} = \frac{W}{2}\begin{pmatrix} \dfrac{2m_F}{2I+1} - \dfrac{1}{2I+1} & \sqrt{1-\left(\dfrac{2m_F}{2I+1}\right)^2} \\ \sqrt{1-\left(\dfrac{2m_F}{2I+1}\right)^2} & -\dfrac{2m_F}{2I+1} - \dfrac{1}{2I+1} \end{pmatrix} \tag{4}$$

whose eigenvalues are $W[I/(2I + 1)]$ and $-W[(I + 1)/(2I + 1)]$, independent of $m_F$. Note that these eigenvalues are not equal in magnitude. Instead, it is the center of gravity of the whole hyperfine multiplet that lies at zero energy.

The $2 \times 2$ blocks of the total energy matrix $E_{unc} + E_{\mathrm{HFS},m_F}$ can be conveniently separated into the sum of two matrices, one with zero trace ad the other proportional to the identity matrix $\mathbb{I}$

$$\frac{W}{2}\left[\begin{pmatrix} x + \dfrac{2m_F}{2I+1} & \sqrt{1-\left(\dfrac{2m_F}{2I+1}\right)^2} \\ \sqrt{1-\left(\dfrac{2m_F}{2I+1}\right)^2} & -x - \dfrac{2m_F}{2I+1} \end{pmatrix} + \left(-\frac{1}{2I+1} + 2\frac{g_I}{g_J - g_I}m_F x\right)\mathbb{I}\right] \tag{5}$$

Note that this expression remains quantitatively correct for the two states that remain uncoupled, $m_F = \pm(I + 1/2)$, although they do not belong to the same $m_F$ block. For these two states, one has

$$\frac{W}{2}\left[\begin{pmatrix} x+1 & 0 \\ 0 & -x+1 \end{pmatrix} + \left(-\frac{1}{2I+1} + 2\frac{g_I}{g_J - g_I}m_F x\right)\mathbb{I}\right] \tag{6}$$

Diagonalization of eq 5 leads to the Breit−Rabi formula

$$E = \frac{W}{2}\left[-\frac{1}{2I+1} + 1 \pm x + 2\frac{g_I}{g_J - g_I}m_F x\right] \qquad |m_F| = I + \frac{1}{2} \tag{7}$$

$$= -\frac{1}{2I+1} + 2\frac{g_I}{g_J - g_I}m_F x \pm \sqrt{1 + \frac{4m_F}{2I+1}x + x^2} \qquad |m_F| < I + \frac{1}{2} \tag{8}$$

and the $\pm$ signs go with the sign of $m_J$. From eq 5, it is easy to see that at large $x$, the separation between two adjacent levels ($\Delta m_J = 0$, $\Delta m_I = 1$,$\Delta m_F = 1$) is $(W\Delta m_F)/(2I + 1) = a_{HFS}/2$.

## References and Notes


(1) Goyal, S.; Schutt, D. L.; Scoles, G. *Phys. Rev. Lett.* **1992**, *69*, 933.
(2) Hartmann, M.; Mielke, F.; Toennies, J. P.; Vilesov, A. F.; Benedek, G. *Phys. Rev. Lett.* **1996**, *76*, 4560.
(3) Grebenev, S.; Toennies, J. P.; Vilesov, A. F. *Science* **1998**, *279*, 2083.
(4) Higgins, J.; Callegari, C.; Reho, J.; Stienkemeier, F.; Ernst, W. E.; Lehmann, K. K.; Gutowski, M.; Scoles, G. *Science* **1996**, *273*, 629.
(5) Nauta, K.; Miller, R. E. *Science* **1999**, *283*, 1895–1897.
(6) Hartmann, M.; Miller, R. E.; Toennies, J. P.; Vilesov, A. *Phys. Rev. Lett.* **1995**, *75*, 1566.
(7) Higgins, J.; Callegari, C.; Reho, J.; Stienkemeier, F.; Ernst, W. E.; Gutowski, M.; Scoles, G. *J. Phys. Chem. A* **1998**, *102*, 4952.
(8) Choi, M. Y.; Douberly, G. E.; Falconer, T. M.; Lewis, W. K.; Lindsay, C. M.; Merritt, J. M.; Stiles, P. L.; Miller, R. E. *Int. Rev. Phys. Chem.* **2006**, *25*, 15.
(9) Field, R. W.; Bradford, R. S.; Harris, D. O.; Broida, H. P. *J. Chem. Phys.* **1972**, *56*, 4712.
(10) Field, R. W.; Bradford, R. S.; Broida, H. P.; Harris, D. O. *J. Chem. Phys.* **1972**, *57*, 2209.
(11) Field, R. W.; English, A. D.; Tanaka, T.; Harris, D. O.; Jennings, D. A. *J. Chem. Phys.* **1973**, *59*, 2191.
(12) Ernst, W. E.; Törring, T. *Phys. Rev. A* **1982**, *25*, 1236.
(13) Rabi, I. I.; Zacharias, J. R.; Millman, S.; Kusch, P. *Phys. Rev.* **1938**, *53*, 318.
(14) Rabi, I. I.; Millman, S.; Kusch, P.; Zacharias, J. R. *Phys. Rev.* **1939**, *55*, 526.
(15) Kellogg, J. M. B.; Rabi, I. I.; Ramsey, N. F.; Zacharias, J. R. *Phys. Rev.* **1939**, *56*, 728.
(16) Kusch, P.; Millman, S.; Rabi, I. I. *Phys. Rev.* **1940**, *57*, 765.
(17) Bethlem, H. L.; Berden, G.; Meijer, G. *Phys. Rev. Lett.* **1999**, *83*, 1558.
(18) Rosner, S. D.; Holt, R. A.; Gaily, T. D. *Phys. Rev. Lett.* **1975**, *35*, 785.
(19) Ertmer, W.; Hofer, B. *Z. Phys. A* **1976**, *276*, 9.
(20) Childs, W. J.; Poulsen, O.; Goodman, L. S. *Phys. Rev. A* **1979**, *19*, 160.
(21) Childs, W. J.; Poulsen, O.; Goodman, L. S.; Crosswhite, H. *Phys. Rev. A* **1979**, *19*, 168.
(22) Yokozeki, A.; Muenter, J. S. *J. Chem. Phys.* **1980**, *72*, 3796.
(23) Ernst, W. E.; Kindt, S.; Törring, T. *Phys. Rev. Lett.* **1983**, *51*, 979.
(24) Brossel, J.; Kastler, A. *Compt. Rend.* **1949**, *229*, 1213.
(25) Kastler, A. *J. Phys. Radium* **1950**, *11*, 255.
(26) Carver, T. R. *Science* **1963**, *141*, 599.
(27) Reinhard, I.; Callegari, C.; Conjusteau, A.; Lehmann, K. K.; Scoles, G. *Phys. Rev. Lett.* **1999**, *82*, 5036.
(28) Conjusteau, A.; Callegari, C.; Reinhard, I.; Lehmann, K. K.; Scoles, G. *J. Chem. Phys.* **2000**, *113*, 4840.
(29) Stienkemeier, F.; Higgins, J.; Callegari, C.; Kanorsky, S. I.; Ernst, W. E.; Scoles, G. *Z. Phys. D* **1996**, *38*, 253.
(30) Bartelt, A.; Close, J. D.; Federmann, F.; Quaas, N.; Toennies, J. P. *Phys. Rev. Lett.* **1996**, *77*, 3525.
(31) Nauta, K.; Miller, R. E. *Phys. Rev. Lett.* **1999**, *82*, 4480.
(32) von Haeften, K.; Metzelthin, A.; Rudolph, S.; Staemmler, V.; Havenith, M. *Phys. Rev. Lett.* **2005**, *95*, 215301.
(33) Herzberg, G. *Infrared and raman spectra of polyatomic molecules*, 2nd ed.; R.E. Krieger Publishing Company: Malabar, FL, 1991; Vol. 2.
(34) Harms, J.; Hartmann, M.; Sartakov, S.; Toennies, J. P.; Vilesov, A. *J. Mol. Spectrosc.* **1997**, *185*, 204.
(35) Callegari, C.; Conjusteau, A.; Reinhard, I.; Lehmann, K. K.; Scoles, G. *J. Chem. Phys.* **2000**, *113*, 10535.
(36) Callegari, C.; Lehmann, K. K.; Schmied, R.; Scoles, G. *J. Chem. Phys.* **2001**, *115*, 10090.
(37) Nauta, K.; Miller, R. E. *J. Chem. Phys.* **2001**, *115*, 8384.
(38) Nauta, K.; Miller, R. E. *J. Chem. Phys.* **2001**, *115*, 10254.
(39) Nauta, K.; Miller, R. E. *Chem. Phys. Lett.* **2001**, *350*, 225.
(40) Piepho, S. B.; Schatz, P. N. *Group theory in spectroscopy: with applications to magnetic circular dichroism*; Wiley-Interscience monographs in chemical physics; Wiley: New York, 1983.
(41) Nagl, J.; Auböck, G.; Callegari, C.; Ernst, W. E. *Phys. Rev. Lett.* **2007**, *98*, 075301.
(42) Auböck, G.; Nagl, J.; Callegari, C.; Ernst, W. E. *J. Phys. Chem. A* **2007**, *111*, 7404.
(43) Auböck, G.; Nagl, J.; Callegari, C.; Ernst, W. E. *J. Chem. Phys.* **2008**, *129*, 114501.
(44) Auböck, G.; Nagl, J.; Callegari, C.; Ernst, W. E. *Phys. Rev. Lett.* **2008**, *101*, 035301.
(45) Arimondo, E.; Inguscio, M.; Violino, P. *Rev. Mod. Phys.* **1977**, *49*, 31.
(46) Breit, G.; Rabi, I. I. *Phys. Rev.* **1931**, *38*, 2082.
(47) Islam, M. A.; Kponou, A.; Suleman, B.; Happer, W. *Phys. Rev. Lett.* **1981**, *47*, 643.
(48) Mattison, E. M.; Pritchard, D. E.; Kleppner, D. *Phys. Rev. Lett.* **1974**, *32*, 507.
(49) Cooke, W. E.; Freeman, R. R. *Phys. Rev. A* **1977**, *16*, 2211.

(50) Davis, R. E.; Muenter, J. S. *J. Chem. Phys.* **1974**, *61*, 2940.
(51) Salerno, L. J.; Kittel, P.; Spivak, A. L. *Cryogenics* **1993**, *33*, 1104.
(52) Ralchenko, Y.; Kramida, A.; Reader, J.; NIST atomic spectra database, v. 3.1.5, online; NIST ASD Team: Gaithersburg, MD, http://physics.nist.gov/asd3 (2009).
(53) Poole, C. P., Jr. *Electron Spin Resonance: A Comprehensive Treatise on Experimental Techniques*; Dover Publications, Inc.: Mineola, NY, 1983.
(54) Stienkemeier, F.; Higgins, J.; Ernst, W. E.; Scoles, G. *Phys. Rev. Lett.* **1995**, *74*, 3592.
(55) Callegari, C.; Higgins, J.; Stienkemeier, F.; Scoles, G. *J. Phys. Chem. A* **1998**, *102*, 95.
(56) Harms, J.; Toennies, J. P.; Dalfovo, F. *Phys. Rev. B* **1998**, *58*, 3341.
(57) Reho, J.; Higgins, J.; Callegari, C.; Lehmann, K. K.; Scoles, G. *J. Chem. Phys.* **2000**, *113*, 9686.
(58) Reho, J.; Higgins, J.; Lehmann, K. K.; Scoles, G. *J. Chem. Phys.* **2000**, *113*, 9694.
(59) Bünermann, O.; Droppelmann, G.; Hernando, A.; Mayol, R.; Stienkemeier, F. *J. Phys. Chem. A* **2007**, *111*, 12684.
(60) Brühl, F. R.; Trasca, R. A.; Ernst, W. E. *J. Chem. Phys.* **2001**, *115*, 10220.
(61) Adrian, F. J. *J. Chem. Phys.* **1960**, *32*, 972–981.
(62) Koch, M.; Auböck, G.; Callegari, C.; Ernst, W. E. *Phys. Rev. Lett.* **2009**, *103*, 035302.
(63) Sakurai, J. J. *Modern quantum mechanics*; Addison-Wesley: Reading, MA, 1993.

JP9041827